Journal Pre-proofs

Crystallinity engineering of Fe_xO through doping and ligand design for improved oxygen Catalysis in Zinc-Air batteries

Jiao Peng, Fangfang Liu, Xinjie Huang, Lijuan Feng, Hui Wang, Xuyun Wang, Jianwei Ren, Rongfang Wang

PII: S1385-8947(25)02919-5
DOI: https://doi.org/10.1016/j.cej.2025.162093
Reference: CEJ 162093

To appear in: *Chemical Engineering Journal*

Received Date: 28 January 2025
Revised Date: 23 March 2025
Accepted Date: 27 March 2025

Please cite this article as: J. Peng, F. Liu, X. Huang, L. Feng, H. Wang, X. Wang, J. Ren, R. Wang, Crystallinity engineering of Fe_xO through doping and ligand design for improved oxygen Catalysis in Zinc-Air batteries, *Chemical Engineering Journal* (2025), doi: https://doi.org/10.1016/j.cej.2025.162093

Crystallinity Engineering of Fe_xO through Doping and Ligand Design for Improved Oxygen Catalysis in Zinc-Air Batteries

Jiao Peng[a], Fangfang Liu[b], Xinjie Huang[a], Lijuan Feng [b], Hui Wang[a,*], Xuyun Wang[a], Jianwei Ren[c,*], Rongfang Wang[a,*]

[a] College of Chemical Engineering, Qingdao University of Science and Technology, Qingdao, 266042, China

[b] Shandong Peninsula Blue Economy and Engineering Research Institute, Weifang University of Science and Technology, Shandong Engineering Laboratory for Clean Utilization of Chemical Resources, Weifang, 262700, China

[c] Department of Chemical Engineering, University of Pretoria, cnr Lynnwood Road and Roper Street, Hatfield 0028, South Africa.

*Corresponding authors: wanghui3931@126.com (H. Wang), rfwang@qust.edu.cn (R. Wang), jianwei.ren@up.ac.za (J. Ren)

Graphical Abstract

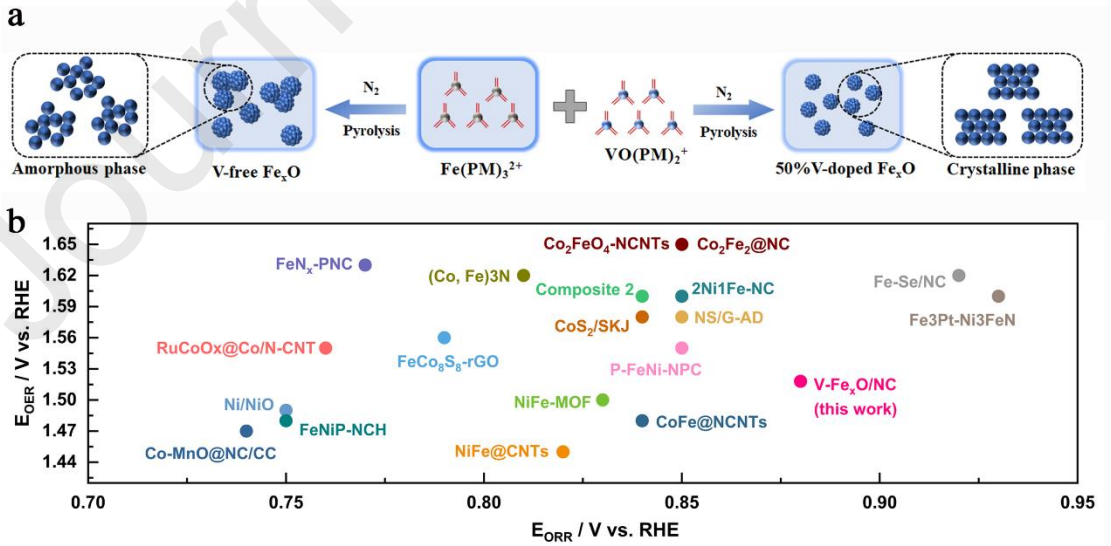

Highlights

- Vanadium (V) doping and the introducing of nitrogen-containing ligands enhance the crystallinity of Fe_xO nanoparticles
- High crystallinity Fe_xO nanoparticles facilitate rapid charge transfer and improve the conductivity of the catalyst.
- The orderly arrangement of metal atoms in the Fe_xO crystal structure effectively enhances the overall stability of the material.
- At 10 mA cm^{-2}, the initial voltage attenuation rate of the V-FexO/NC-based ZAB was 93.6% after 280 h of discharge.

Abstract:

The crystallinity of metal oxides plays a pivotal role in regulating the arrangement of metal atoms and thereby influencing electrocatalytic performance. This study focuses on carbon-supported transition metal oxide catalysts (V-Fe_xO/NC) and investigates how improved crystallinity impacts their performance in both oxygen evolution reaction (OER) and oxygen reduction reaction (ORR). It is demonstrated that doping with vanadium (V) and introducing nitrogen-containing ligands enhance the crystallinity of Fe_xO nanoparticles in the V-Fe_xO/NC catalyst. The high crystallinity of Fe_xO facilitates efficient electron transfer within the material and sequentially resulting in superior electrical conductivity. Furthermore, electron paramagnetic resonance (EPR) analysis suggests a lower concentration of oxygen vacancies in V-Fe_xO/NC sample, attributed to the well-ordered crystalline structure of Fe_xO, which

minimizes internal defects and improves catalyst stability. As a result, the V-Fe_xO/NC composite demonstrates exceptional electrocatalytic efficiency, evidenced by a potential gap of merely 0.64 V, which surpasses the performance of the Pt/C+RuO_2 catalyst (0.66 V), while also exhibiting outstanding durability in both ORR and OER processes. Zinc-air batteries incorporated with V-Fe_xO/NC exhibit a stable open-circuit voltage (1.46 V) and high specific capacity (743.0 mAh g^{-1}).

Keywords: High crystallinity; Fe_xO nanoparticles; Oxygen electrocatalyst; Zinc-air batteries

1. Introduction

To meet the increasing need for sustainable energy storage solutions, rechargeable zinc-air batteries (ZABs) have emerged as highly promising devices for clean and efficient energy conversion [1, 2]. Nevertheless, the cathodic processes in zinc-air batteries, including the oxygen reduction reaction (ORR) as well as oxygen evolution reaction (OER), involve complex proton-coupled electron transfer mechanisms. These multi-step reactions exhibit slow kinetics, which significantly limit the total performance of the batteries [3]. Given that noble metal catalysts like Pt and Ir perform excellent in catalytic activity, their practical application is constrained by factors including limited availability, high cost, and poor stability [4]. As a result, the development of affordable and high-efficiency non-precious metal catalysts is crucial for enhancing the performance of zinc-air batteries. Among these, transition metal oxides (TMOs), particularly iron-based oxides, have garnered significant interest in electrocatalysis. This is attributed to their rich 3d electron configurations, exceptional catalytic activity, robust stability, and easily adjustable valence states [5, 6]. In recent years, numerous approaches have been introduced to improve the catalytic efficiency of TMOs, including nanostructure design, elemental doping, and crystal phase engineering, all of which have been extensively explored [7-9] . One of the most effective strategies involves regulating crystallinity, which optimizes the

spatial arrangement of metal atoms. Adjusting crystallinity significantly influences surface adsorption properties and charge distribution, thereby enhancing electrical conductivity and catalytic activity [10-12]. For example, Jiang et al. [13] demonstrated a crystallinity-tuning strategy to improve the OER performance of electrocatalysts. They developed Ni-Bi@NB composite as a highly efficient OER catalyst, in which nickel boride (Ni_3B) nanoparticles as the core and nickel(II) borate (Ni-Bi) as the shell. Their findings revealed that partially crystalline Ni-Bi exhibited superior activity, with reduced electrochemical impedance and increased per-site activity as Ni-Bi transitioned from an amorphous to a polycrystalline state. This catalyst achieved a low overpotential of 302 mV at 10 mA cm^{-2} and exhibited a Tafel slope of 52 mV dec^{-1}. Hu and co-workers [14] reported that well-crystallized FeNi alloys supported on a carbon shell combined with an active FeO_y layer exhibited enhanced electronic conductivity and synergistic interfacial effects, significantly boosting the intrinsic activity of the oxygen electrocatalyst. Additionally, Hu et al. [15] synthesized a high-crystallinity bi-nuclear phthalocyanine iron (bi-FePc) encapsulated in multi-walled carbon nanotubes (bi-FePc/MWNT). This material displayed exceptional performance as an ORR electrocatalyst, maintaining stable current density after 14 h of chronoamperometric testing, indicative of its outstanding stability. Furthermore, studies have shown that in iron-based oxides and hydroxide catalysts, β-FeOOH(Cl) nanorods with reduced dimensions and high crystallinity exhibit the best OER activity. Specifically, the highly crystalline β-FeOOH enhanced current density, whereas low-crystallinity β-FeOOH displayed inferior OER performance [16]. These findings underscore the critical influence of crystallinity on OER catalytic performance.

This study presents the synthesis of an efficient oxygen electrocatalyst (V-Fe_xO/NC) through a straightforward pyrolysis method. The catalyst comprises Fe_xO nanoparticles and vanadium anchored onto a porous carbon framework. Notably, the

crystallinity of Fe_xO significantly impacts its oxygen catalytic activity. The incorporation of phenanthroline (PM) as a nitrogen-containing ligand effectively anchors metal ions during synthesis. The results reveal that the synthesized V-Fe_xO/NC contains highly crystalline Fe_xO particles, which reduce electron transfer resistance and facilitate charge transport within the material, thereby enhancing electrical conductivity. Additionally, the well-crystallized Fe_xO minimizes defects and vacancies within the crystal structure, resulting in improved structural integrity and cycling stability. Consequently, the highly crystalline V-Fe_xO/NC catalyst exhibits outstanding catalytic performance and long-term stability for both ORR and OER. It attains an impressive $E_{1/2}$ of 0.88 V and a minimal overpotential of only 288 mV at 10 mA cm^{-2} current density. When V-Fe_xO/NC is incorporated, the assembled battery exhibits outstanding durability, with an 93.6% initial voltage retention rate after continuous discharge for 280 h, highlighting its significant potential for practical applications.

2. Experimental

2.1. N-Doped Porous Carbon (NC) sample

The NC sample was synthesized as follows: 1 g of peptone was carefully blended with 10 g of calcium chloride using ball milling for 1.5 h. The resulting mixture was then placed in a tubular furnace and heated under a nitrogen (N_2) flow. The temperature was gradually raised to 900 °C at 5 °C/min, held for 1 h and subsequently cooled to 20 °C. The obtained sample was repeatedly washed with water and then subjected to three rounds of acid washing using 50 mL of hydrochloric acid (HCl, 1 M). Finally, the sample was rinsed with water several times to produce the NC material.

2.2. V-Fe_xO/NC, Fe_xO/NC, and V/NC samples

The V-Fe_xO/NC catalyst was synthesized using NC, $FeCl_2 \cdot 4H_2O$, NH_4VO_3, and PM ($C_{12}H_8N_2 \cdot H_2O$) as raw materials in deionized water. Initially, 80 mg of NC was mixed

in 5 mL of deionized water to form a colloidal solution. Subsequently, 0.15 mL (0.015 mmol) of $Fe(PM)_3^{2+}$ solution and 0.15 mL (0.015 mmol) of $VO(PM)_2^{+}$ solution were added under stirring for 1 h. Afterwards, the mixture was dried in an oven at 60 °C for 3 h. The dried sample was subsequently heat-treated at 800 °C for 1 h in a tube furnace under N_2 protection. After cooling to room temperature, the resulting product was labeled as V-Fe_xO/NC.

Under identical conditions, Fe_xO/NC and V/NC were synthesized by pyrolyzing $Fe(PM)_3^{2+}$ and $VO(PM)_2^{+}$, respectively.

The solution of 0.1 M $Fe(PM)_3^{2+}$ was obtained through dissolving 0.198 g of $FeCl_2 \cdot 4H_2O$ and 0.595 g of PM in 10 mL of water. Similarly, the solution of 0.1 M $VO(PM)_2^{+}$ was prepared via mixing 0.117 g of NH_4VO_3 and 0.397 g of PM in 10 mL of water.

2.3. Other Samples

The molar ratio of Fe to V in V-Fe_xO/NC-X **(Table S1)** was varied under identical conditions to understand the effect of Fe/V ratio. The temperature effect of pyrolysis was also examined on the properties of V-Fe_xO/NC-T_x **(Table S2)** under the optimal molar ratio conditions. Detailed information regarding these parameters is provided in the Supporting Information.

3. Results and Discussion

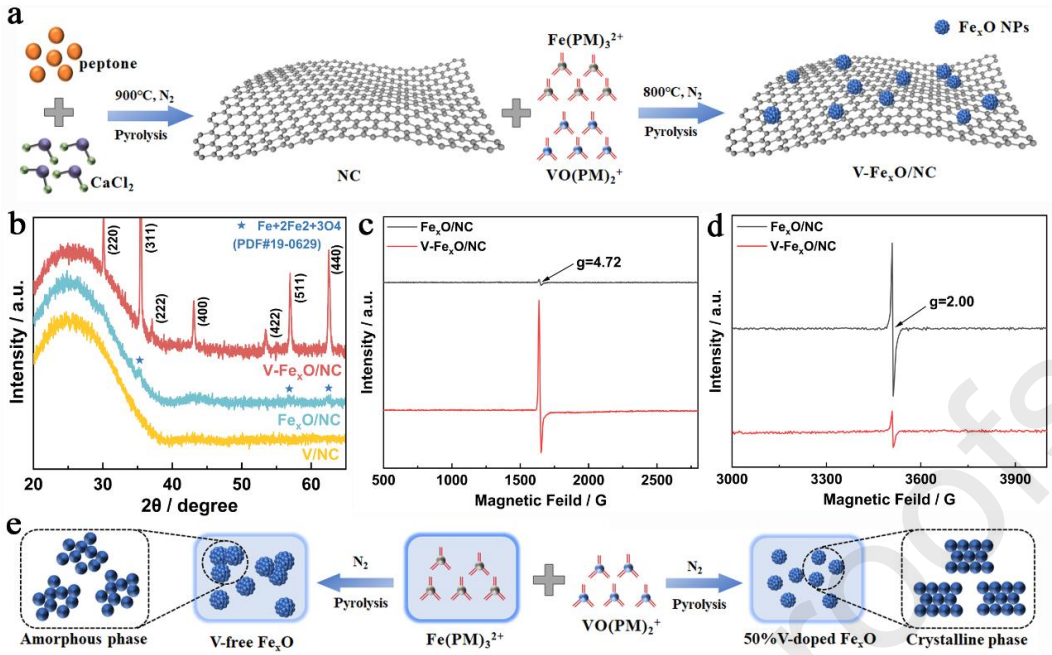

Fig. 1. (a) Schematic process for preparing V-Fe_xO/NC sample. (b) XRD pattern of V-Fe_xO/NC sample. (c) EPR spectrum of Fe^{2+} at g = 4.72. (d) EPR spectrum of oxygen vacancies at g = 2.0. (e) Schematic of the modulation of Fe_xO crystallinity.

Fig. 1a illustrates the key steps in the synthesis of the V-Fe_xO/NC catalyst. The NC substrate was first prepared via pyrolysis after mixing peptone and calcium chloride by ball milling. The metal ions were chelated with PM to facilitate their effective anchoring on the porous carbon framework. A second pyrolysis step was performed to obtain the V-Fe_xO/NC catalyst containing highly crystalline Fe_xO nanoparticles. The prepared catalyst samples were characterized in **Fig. 1b** through X-ray diffraction (XRD) analysis. It is evident that all samples display a broad diffraction peak near 25.1°, which corresponds to the (002) plane of amorphous carbon (PDF#41-1487) [17]. The characteristic peaks at 30.10°, 35.42°, 43.05°, 56.94°, and 62.52° in the V-Fe_xO/NC sample are attributed to Fe+2Fe2+3O4 (PDF#19-0629) at the (220), (311), (400), (511), and (440) planes, respectively. However, the Fe_xO/NC sample shows only faint diffraction peaks for Fe+2Fe2+3O4, indicating poor crystallinity. No V-related diffraction peaks are observed in the V-Fe_xO/NC and V/NC samples, suggesting that V exists in an amorphous state. Through Lorentzian function fitting of

the diffraction peak of Fe+2Fe2+3O4 in the XRD pattern (**Tables S3–S4**), it was found that the full width at half maximum (FWHM) of the (311) plane of Fe_xO/NC is 2.49°, while the FWHM of V-Fe_xO/NC significantly decreased to 0.18°. This indicates that V-doping effectively improves the atomic arrangement and order. The introduction of V also caused a shift in the diffraction peak of the (311) plane from 35.1° to 35.5°. Based on Bragg's law, it was calculated that the d-spacing of the crystal plane decreased by 0.004 nm, and the lattice constant (a) shrunk from 8.36 Å to 8.20 Å, indicating that a small amount of V was incorporated into Fe_xO. Furthermore, according to the Scherrer equation, it was calculated that the average crystallite size of Fe_xO increased significantly from 8.6 nm (without V-doping) to 40.9 nm with V-doping. This suggests that V-doping not only promotes the ordered growth of the crystallites but also reduces the grain boundary density and facilitates the rapid transfer of charges. Additionally, the XRD patterns of samples prepared by different pyrolysis temperatures **(Fig. S1**) indicate the presence of diffraction peaks for Fe+2Fe2+3O4, with increased crystallinity as the pyrolysis temperature rises. Electron paramagnetic resonance (EPR) spectroscopy was deployed to examine the transition metal valence states and defect levels in the samples. **Fig. 1c** shows a peak near a g-factor of 4.27, which is assigned to Fe^{2+}. The V-Fe_xO/NC sample exhibits a higher concentration of Fe^{2+} compared to other samples. **Fig. 1d** presents a peak at a g-factor of 2.0, corresponding to oxygen vacancy defects. Notably, the weak oxygen vacancy signal in V-Fe_xO/NC suggests a low concentration of oxygen defects in this sample [18]. This result is mainly attributed to the high crystallinity of Fe_xO in V-Fe_xO/NC, which possesses an intact crystal structure and effectively reduces defect formation. **Fig. 1e** illustrates the differences in crystallinity of the synthesized Fe_xO particles. During the synthesis, the doping of V and the efficient metal anchoring by the nitrogen-containing PM ligand led to the successful formation of highly crystalline Fe_xO particles, where the metal atoms exhibited a highly ordered

arrangement. In contrast, the Fe_xO with lower crystallinity displayed a disordered arrangement of metal atoms.

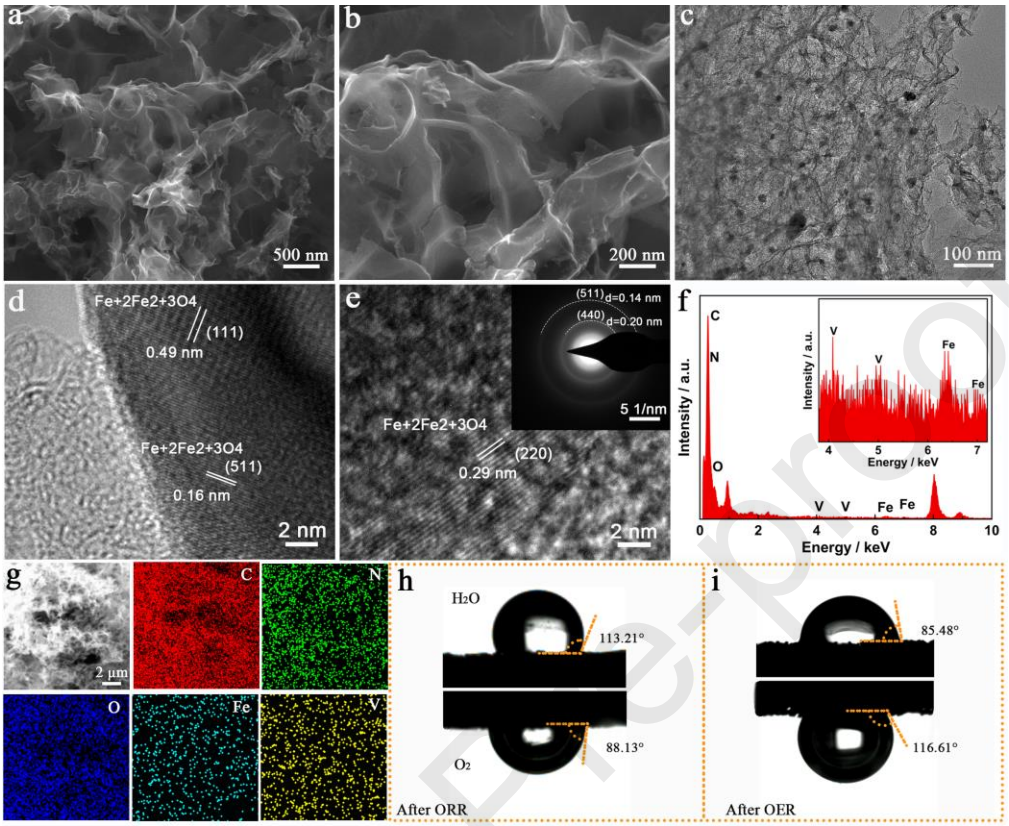

Fig. 2. (a–b) SEM images of V-Fe_xO/NC sample. (c) TEM image of V-Fe_xO/NC sample. (d–e) HRTEM images of V-Fe_xO/NC sample, with SAED pattern (e inset). (f) EDS elemental spectrum with enlarged pattern (inset). (g) Elemental mapping images. (h–i) Water and bubble contact angle measurements after 3 h of reaction at ORR and OER potentials, respectively.

The scanning electron microscopy (SEM) images from V-Fe_xO/NC sample are presented in **Fig. 2a–b.** The three-dimensional open nanostructure expose more active sites and accelerates the mass as well as charge transport [19]. The transmission electron microscopy (TEM) images in both **Fig. 2c** and **Fig. S2a** reveal well-dispersed metal particles within V-Fe_xO/NC. The average particle size of the Fe_xO nanoparticles in V-Fe_xO/NC was calculated to be 10.6 nm (**Fig. S2b**). The further high-resolution transmission electron microscopy (HRTEM) images in **Fig. 2d–e** clearly display

lattice spacing values of 0.49, 0.16 and 0.29 nm. They are corresponding to the (111), (511), and (220) planes of Fe+2Fe2+3O4, respectively. The two diffraction rings observed in the selected area electron diffraction (SAED) pattern (**Fig. 2e**, inset**)** correspond to the (440) and (511) planes of Fe+2Fe2+3O4, with interplanar spacings of 0.20 nm and 0.14 nm, respectively. Therefore, this observation goes well with the XRD results by confirming the high crystallinity of Fe_xO nanoparticles in V-Fe_xO/NC sample. Additionally, the TEM images of Fe_xO/NC sample in **Fig. S3** exhibit nanoparticles of varying sizes with severe agglomeration. In comparison, the particle size of Fe_xO/NC is significantly larger at 7.07 nm (**Fig. S3b**) than that of V-Fe_xO/NC. This phenomenon suggests that the doping of V and the anchoring effect of the ligand reduce the particle size, resulting in a high-density distribution of active sites within the carbon matrix and significantly mitigating the agglomeration of metal particles. The energy dispersive spectroscopy (EDS) spectrum (**Fig. 2f**) confirms the presence of various elements in the V-Fe_xO/NC catalyst. In the inset of **Fig. 2f**, the characteristic peaks of V and Fe can be further observed. The quantitative EDS analysis (**Table S5**) shows that the weight percentages of V and Fe in V-Fe_xO/NC are 0.20% and 0.32%, respectively. This confirms the presence of V and Fe in the V-Fe_xO/NC composite sample. The elemental mapping (**Fig. 2g**) further shows that C, N, O, V and Fe are the major components of the catalyst. Contact angle measurements were performed to evaluate the mass transport effects during ORR and OER. As illustrated in **Fig. 2h**, the contact angle of oxygen on sample surface was 88.13° after 3 h of the ORR process, which implies that O_2 can easily reach the solid catalyst layer and promotes mass transport of the oxygen reactants in the gas diffusion layer. After the OER reaction, the water contact angle on the electrode surface decreased to 85.48° (**Fig. 2i**). Clearly, the hydrophilicity increases in comparison to the water contact angle of 113.1° during the ORR process. This promotes better contact between the catalyst layer and the electrolyte. Moreover, the contact angle of oxygen bubbles increased by approximately 28.48°, providing a fast gas diffusion channel for O_2 [20].

Therefore, the V-Fe_xO/NC catalyst is expected to achieve a well-balanced gas-liquid mass transfer within the catalytic layer during the ORR/OER processes.

Raman spectroscopy further revealed two distinct peaks in the samples (**Fig. S4a**), and they are corresponding to the G band (sp^2 hybridized carbon) and D band (disordered graphite structure) of the carbon structure, respectively. The D band appears at 1374.8 cm^{-1}, while the G band is located around 1594.5 cm^{-1}. The defect density of the materials was evaluated by calculating the intensity ratio of I_D/I_G. The I_D/I_G ratios for V-Fe_xO/NC and Fe_xO/NC samples were 0.99 and 0.92, respectively. The higher I_D/I_G ratio in V-Fe_xO/NC indicates a greater number of carbon structure defects. A higher density of edge defects is beneficial for enhancing inherent charge activity, which positively impacts the material's performance [21]. In addition, the specific surface area and pore structure of the samples were determined through analysis using a BET analyzer. As displayed in **Fig. S4b**, all samples exhibit an IV-type N_2 adsorption-desorption isotherm, which suggests the co-presence of both micropores and mesopores within the material [22]. This observation is consistent with the pore size distribution from **Fig. S4c**. More specifically, The V-Fe_xO/NC sample in **Fig. S4d** displays a larger BET surface area (864.41 m^2 g^{-1}) and a relatively higher pore volume (1.08 cm^3 g^{-1}). **Fig. S5** shows that the two parameters increase with the rising pyrolysis temperatures. The enhanced surface area of the V-Fe_xO/NC sample is anticipated to reveal a greater number of active sites and accessible O_2 diffusion sites [23]. The abundant pore structure of the V-Fe_xO/NC sample will enable improved electrolyte to contact with the catalyst surface, thereby promoting the adsorption of reactants and the dissociation of intermediates [24].

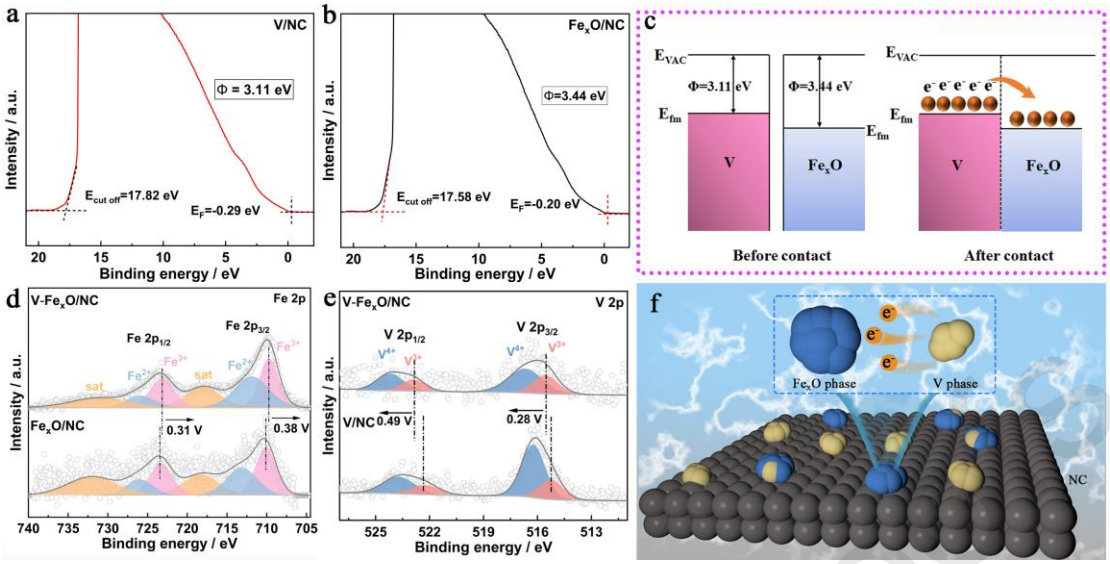

Fig. 3 (a–b) UPS spectra of V/NC and Fe_xO/NC catalysts. (c) Diagram of electron transfer before and after contact between V/NC and Fe_xO/NC. XPS spectra of (d) Fe 2p and (e) V 2p. (f) Schematic illustration of the inter-metal electron transfer.

The work function (Φ) of V/NC and Fe_xO/NC catalysts was calculated using ultraviolet photoelectron spectroscopy (UPS) to be 5.70 eV and 5.95 eV, respectively (**Fig. 3a–b**). The difference in the Fermi energy levels between the two is a necessary condition for the interfacial electron transfer observed in V-Fe_xO/NC (**Fig. 3c**). In other words, the lower Φ of V/NC requires a reduced energy barrier for electron transfer between oxygen intermediates and catalyst surface [25]. This not only results in the formation of iron in lower oxidation states but may also cause a downward bending of the conduction along with valence bands in the Fe_xO phase [26]. The full X-ray photoelectron spectroscopy (XPS) spectrum of V-Fe_xO/NC sample in **Fig. S6a** shows the presence of C, N, O, V, and Fe elements. **Fig. 3d** illustrates the high-resolution Fe 2p spectrum of V-Fe_xO/NC sample. The peaks at 709.95 eV and 723.39 eV can be attributed to Fe $2p_{3/2}$, Fe $2p_{1/2}$ along the nearby satellite peaks. Specifically, the peaks at 709.72 eV and 723.19 eV are attributed to Fe^{3+}, while those at 711.99 eV and 726.12 eV correspond to Fe^{2+}[27, 28]. Compared with Fe_xO/NC sample, the Fe^{3+} peaks in V-Fe_xO/NC sample shift by about 0.30 eV and 0.38 eV towards lower

binding energies. This indicates that Fe in V-Fe_xO/NC has gained electrons, which reduced its oxidation state and increased the electronic density of Fe-N_x. The high-resolution V 2p XPS spectrum in **Fig. 3e** displays peaks for V $2p_{3/2}$ and V $2p_{1/2}$ at approximately 516.18 eV and 523.28 eV, respectively. The peaks at 515.52 eV and 522.36 eV are assigned to V^{3+}, while those at 516.78 eV and 523.56 eV correspond to V^{4+}[29]. Notably, compared with V/NC sample, the binding energy of V 2p in V-Fe_xO/NC composite shifts to higher binding energies by approximately 0.28 eV and 0.49 eV. This suggests a strong electronic interaction between the bimetallic V and Fe, with electrons transferring from the V sites to the Fe sites. The V-doping effectively regulates the electronic structure of Fe, which is crucial for accelerating catalytic activity [30]. **Fig. 3f** illustrates the process of interfacial electron transfer, which helps reduce the energy barrier for the reaction intermediates, optimizing the adsorption/desorption process of oxygen intermediates, thereby improving ORR and OER electrochemical performance [1, 20]. Similar electron transfer processes have been reported in the literature [31, 32]. Moreover, the high-resolution C1s spectrum (**Fig. S6b**) provides additional evidence of nitrogen doping in the sample, indicated by the presence of the C-N group. The N 1s spectrum in **Fig. S6c** shows four peaks at 397.36 eV, 398.47 eV, 400.21 eV, and 403.64 eV, which belong to pyridinic-N, pyrrolic-N, graphitic-N, and N-oxide, respectively [33]. The binding energy shifts between V-Fe_xO/NC, Fe_xO/NC, and V/NC indicate the electron transfer between metal surface and NC substrate. A comparison of the N species content across the three samples (**Fig. S6d**) reveals that pyridinic-N and graphitic-N together constitute about 66% of the total N content in V-Fe_xO/NC sample. The high content of graphitic-N results in delocalized electron distribution in the carbon, which facilitates the adsorption/desorption process of O-containing species and positively influences the material's electronic conductivity [34]. Additionally, the conductivity values of the prepared samples are recorder in **Fig. S7**. In contrast, V-Fe_xO/NC sample exhibits the highest conductivity value of 10.14 S mm^{-1} among the several catalyst samples, which

facilitates efficient and rapid charge transfer. This can be attributed to the high crystallinity of the Fe_xO nanoparticles and the elevated levels of graphitic nitrogen present within V-Fe_xO/NC sample.

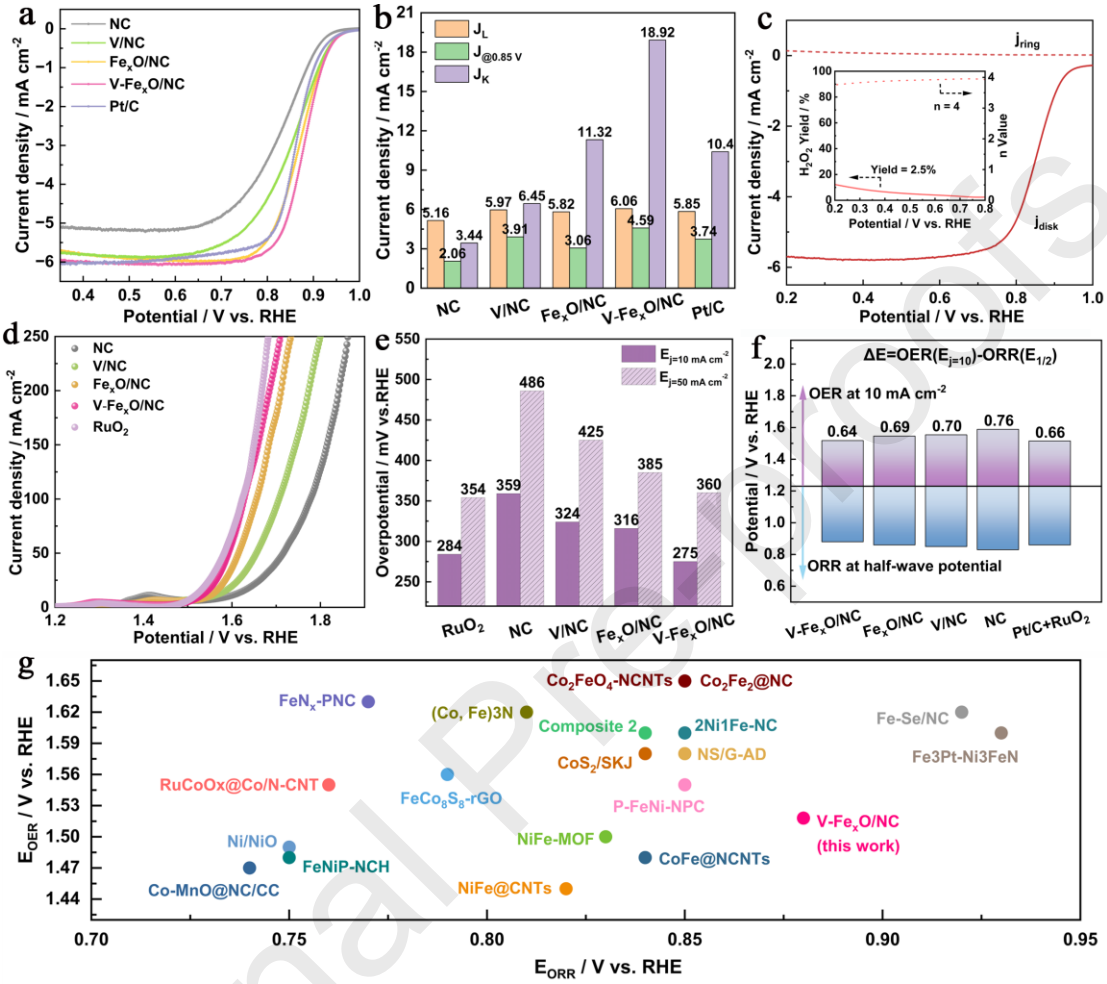

Fig. 4. (a) LSV curves for ORR. (b) The limit current density (J_L), current density at 0.85 V (J@0.85V), and kinetic current density (J_K). (c) The RRDE curve with an inset showing the H_2O_2 yield and electron transfer number. (d) LSV curves for OER. (e) The overpotential values at 10 and 50 mA cm^{-2}. (f) A bar chart of the bifunctional performance, while the inset compares the performance of this study's bifunctional catalysts with those reported in recent literature [21, 30, 35-52].

The ORR catalytic performance of the prepared samples was assessed using a 0.1 M KOH electrolyte. The V-Fe_xO/NC sample exhibits an excellent O_2 reduction ability in **Fig. S8** with the most positive oxygen reduction peak under O_2-saturated

conditions [53]. Clearly, the LSV curves from the V-Fe_xO/NC sample in **Fig. 4a** and **Fig. S9a** show the highest $E_{1/2}$ of 0.88 V, along with a kinetic current density of 18.92 mA cm^{-2} at 0.85 V, outperforming Pt/C ($E_{1/2}$=0.87 V, Jk=10.40 mA cm^{-2}) and other catalyst samples. This indicates that V-doping optimizes the electronic structure of Fe, reconstructs the interfacial charge distribution, and enhances the adsorption of oxygen intermediates, thereby improving its ORR catalytic activity. **Fig. 4b** compares the current densities of the three samples, showing that V-Fe_xO/NC sample exhibits higher values and surpasses the performance of other catalysts. These results underscore the crucial role of V-doping in enhancing the activity of the ORR pathway. The Tafel curve fitting shown in **Fig. S9b** reveals that the Tafel slope of V-Fe_xO/NC (52.4 mV dec^{-1}) sample is lower than that of Pt/C (64.2 mV dec^{-1}), which suggests that V-Fe_xO/NC sample exhibits a faster electron transfer rate. The incorporation of V-doping enhances the crystallinity of Fe_xO, improves charge transfer capabilities, and effectively optimizes the ORR kinetics of V-Fe_xO/NC. As shown in **Fig. 4c**, the H_2O_2 yield, and electron transfer number (n) were assessed using a rotating ring-disk electrode (RRDE) setup. The inset reveals that the H_2O_2 yield for V-Fe_xO/NC is as low as 2.50%, indicating the catalyst's high selectivity for the intermediate OH^- and its electron transfer number close to 4. The LSV curves at different rotation speeds are presented in **Fig. S10a**, and the electron transfer number (n) is calculated to be 4 in **Fig. S10b** using the Koutecky-Levich (K-L) equation. Therefore, V-Fe_xO/NC facilitates an efficient four-electron transfer process. In evaluating the stability of V-Fe_xO/NC catalyst during the ORR process, the LSV curves before and after 5500 cycles (**Fig. S11**) show that the $E_{1/2}$ of the catalyst decreased by about 18 mV, and this performance results from the high crystallinity of Fe_xO in V-Fe_xO/NC sample, which enhances the structural stability of the material. Furthermore, a comparison of the ORR performance for samples with varying molar ratios of Fe and V-doping (**Fig. S12**) reveals that the V-Fe_xO/NC sample exhibits a high starting potential ($E_{1/2}$) and a

lower Tafel slope. Similarly, catalysts obtained by controlling the pyrolysis temperature confirmed that V-Fe_xO/NC has the best ORR performance (**Fig. S13**).

The OER activity of the catalyst was subsequently investigated in a 1 M KOH electrolyte. The OER LSV curves in **Fig. 4d**, reveal that the V-Fe_xO/NC catalyst exhibits an overpotential of 288 mV at 10 mA cm^{-2} and 360 mV at 50 mA cm^{-2}, respectively, which are comparable to the OER performance of commercial RuO_2 (285 mV, 354 mV) and lower than that of other catalysts (**Fig. 4e**). This indicates that the V-Fe_xO/NC catalyst possesses excellent OER catalytic activity. The electrochemical impedance spectroscopy (EIS) fitting results, depicted in **Fig. S14a**, indicate that the V-Fe_xO/NC catalyst displays the smallest semicircle. This observation implies that V-FexO/NC possesses the lowest charge transfer resistance (R_{ct}), signifying a comparatively higher rate of charge transfer [54]. The OER catalytic kinetics of the catalyst were assessed through Tafel fitting (**Fig. S14b**), and the results show that the Tafel slope of V-Fe_xO/NC (123.0 mV dec^{-1}) is lower than those from RuO_2 (129.7 mV dec^{-1}), indicating faster OER kinetics for V-Fe_xO/NC. The stability of the V-Fe_xO/NC catalyst during the OER process was evaluated through LSV tests after 5500 cycles (**Fig. S15**). The V-Fe_xO/NC catalyst exhibited a minimal shift of only 11 mV at 50 mA cm^{-2}, highlighting its excellent OER stability. The OER performance of samples with different bimetallic molar ratios are tested under identical conditions in **Fig. S16,** where V-Fe_xO/NC once again exhibits the highest OER activity [55]. The bifunctional catalytic efficiency of the electrocatalysts was assessed through the potential difference (△E) between ORR and OER, calculated as $\Delta E = E_j = 10 - E_{1/2}$) (**Fig. 4f**). The V-$Fe_xO$/NC catalyst shows a lower potential difference of 0.64 V compared to that of commercial Pt/C+RuO_2 (ΔE = 0.66 V) and other prepared catalysts. Moreover, compared to recently reported ORR/OER electrocatalysts (**Fig. 4g**, **Table S3**), the V-Fe_xO/NC catalyst exhibits excellent bifunctional oxygen electrocatalytic activity. Double-layer capacitance (C_{dl}) measurements of the catalyst (**Fig. S17**) reveal that V-Fe_xO/NC sample achieves the

highest C_{dl} value of 7.68 mF cm^{-2}, which surpasses the values recorded for V/NC (5.04 mF cm^{-2}), Fe_xO/NC (6.47 mF cm^{-2}), and NC (0.67 mF cm^{-2}) samples. Apparently, V-doping improves the crystallinity of Fe_xO particles and facilitates interfacial charge transport, ultimately increasing the electrochemically active surface area of the V-Fe_xO/NC catalyst. Furthermore, XRD analysis conducted post-ORR and OER in **Fig. S18** confirms that diffraction peaks corresponding to the Fe+2Fe2+3O4 phase (PDF#19-0629) remain present in the V-Fe_xO/NC sample. This signifies that its bulk crystalline structure remains intact without undergoing phase transitions or structural degradation during the reactions. Nevertheless, continuous oxidation-reduction cycling (e.g., $Fe^{3+} \leftrightarrow Fe^{2+}$ transitions) on the material's surface throughout the ORR/OER processes gradually reduces its crystallinity.

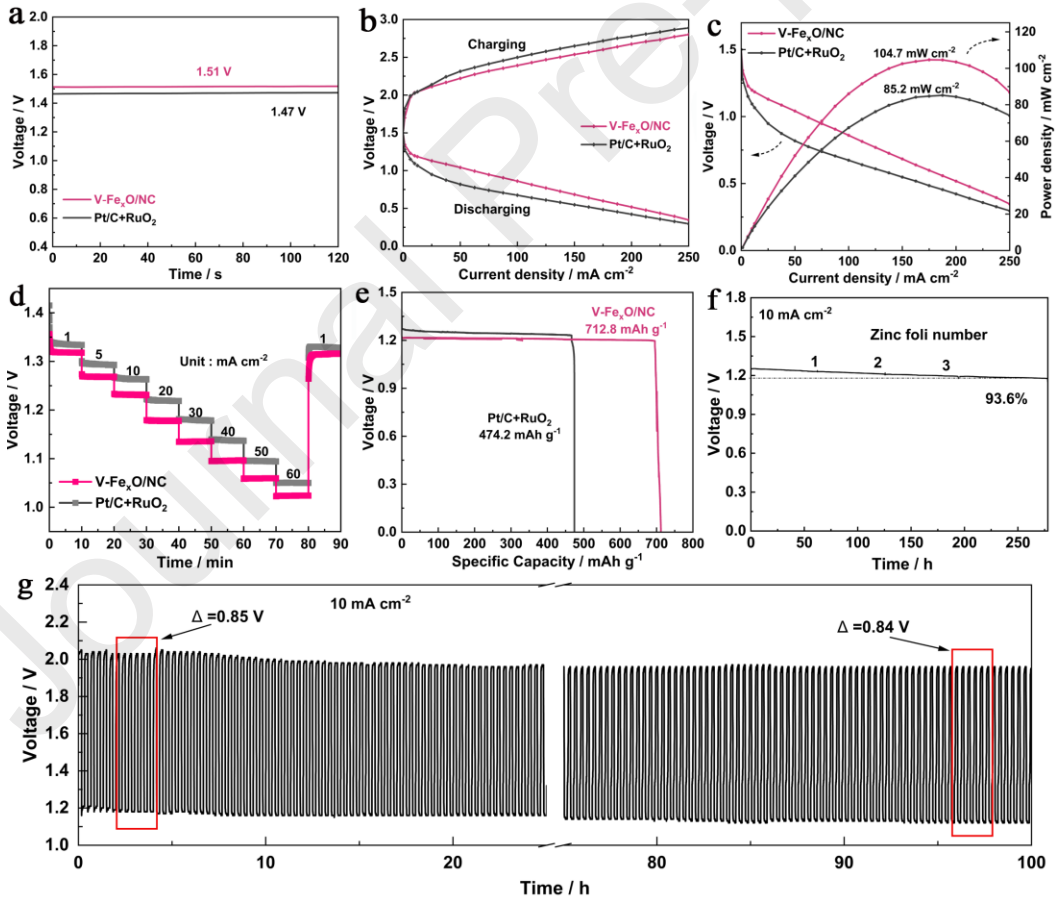

Fig. 5. (a) OCV curves. (b) The charge-discharge polarization curves. (c) The discharge polarization curves and corresponding power density curves. (d) The

variation in battery voltage over time at different current densities. (e) The discharge curve and specific capacity at 10 mA cm^{-2}. (f) The constant current discharge curve. (g) The long-term charge-discharge cycling curves for the V-Fe_xO/NC-based ZAB.

The V-Fe_xO/NC-based ZAB was assembled to test the performance of the catalyst in practical ZABs and the Pt/C + RuO_2-based ZAB was used as a benchmark. As seen, the open circuit voltage (OCV) of the V-Fe_xO/NC-based ZAB (1.51 V) in **Fig. 5a** is higher than that of the Pt/C + RuO_2-based ZAB (1.47 V). The charge-discharge polarization curve of the battery (**Fig. 5b**) reveals that the voltage difference for the V-Fe_xO/NC-based battery is 2.45 V, which is lower than the 2.60 V observed for the Pt/C+ RuO_2-based battery. This suggests that the V-Fe_xO/NC-based battery undergoes reduced energy loss during the charge-discharge cycle. The observed improvement is mainly attributed to V-doping, which promotes the formation of highly crystalline Fe_xO nanoparticles. This modification also alters the local electronic structure of Fe, facilitating a faster charge transfer pathway and enhancing the dual-function catalytic activity in the ZAB. The discharge polarization curves, and the associated power density (**Fig. 5c**) reveal that the V-Fe_xO/NC-based ZAB reaches a peak power density of 104.7 mW cm^{-2}. In contrast, the Pt/C+RuO_2-based ZAB delivers a lower peak power density of 85.2 mW cm^{-2}. These results indicate that V-Fe_xO/NC catalyst demonstrates excellent battery performance [56]. A stable voltage platform is observed in **Fig. 5d** from the V-Fe_xO/NC-based ZAB as the discharge current increases from 1 mA cm^{-2} to 60 mA cm^{-2}. Nearly no voltage decay is noticed when the current density switches from high to low, which suggests an excellent reversibility [57]. Furthermore, discharge tests in **Fig. 5e** show that the specific capacity of the V-Fe_xO/NC-based ZAB is as high as 712.8 mAh g^{-1} at 10 mA cm^{-2}, and this significantly surpasses the Pt/C+RuO_2-based ZAB (474.2 mAh g^{-1}). Remarkably, under the discharge condition of 10 mA cm^{-2}, the V-Fe_xO/NC-based ZAB exhibited excellent stability during a constant current discharge lasting up to 280 h, with an

initial voltage decay rate of only 93.6% (**Fig. 5f**). The long-term charge-discharge cycling curve in **Fig. 5g** indicates that the voltage difference of the V-Fe_xO/NC-based ZAB decreased by only 0.01 V after 100 h of continuous cycling, highlighting the exceptional cycling stability of this battery. This durability is attributed to the strong Fe_xO crystal structure formed through V-doping, which plays a crucial role in preserving the structural integrity of the catalyst and ensuring the battery's stability during prolonged cycling. Moreover, by comparing the performance of the V-Fe_xO/NC-based ZAB with recently reported similar catalyst-based ZABs (**Table S7**), it is confirmed that V-Fe_xO/NC sample exhibits superior bifunctional oxygen activity and application potential in ZABs.

The improved bifunctional oxygen catalytic activity of V-Fe_xO/NC can be attributed to four primary factors. Firstly, the material's three-dimensional nanoscale architecture offers an extensive surface area, effectively accommodating a higher number of active sites [58]. Additionally, the rich porosity of the structure facilitates rapid ion/electron transfer, aiding in efficient gas diffusion/electrolyte mass transport [59]. Secondly, the highly crystalline Fe_xO nanoparticles play a critical role in the material's performance. On one hand, they promote rapid charge transfer, improving the conductivity of the catalyst. On the other hand, the ordered arrangement of metal atoms in the Fe_xO crystal structure effectively enhances the overall stability of the material. Third, V-Fe_xO/NC has a high content of pyridinic nitrogen and graphite nitrogen. Pyridinic nitrogen serves as an effective active site, while graphite nitrogen induces electronic redistribution of surrounding carbon atoms, improving charge transfer. These factors positively impact catalytic activity. Furthermore, a strong electronic interaction is evident between the V and Fe_xO phases in V-Fe_xO/NC in promoting interfacial electron transfer and optimizing the oxygen adsorption as well as activation at the active sites.

4. Conclusion

In summary, this study successfully synthesized a bifunctional oxygen electrocatalyst, V-Fe_xO/NC, through the doping of vanadium (V) and the chelation effect between metal ions and ligands. The results demonstrate that the Fe_xO particles in the V-Fe_xO/NC catalyst exhibit good crystallinity, which significantly improves the material's conductivity while enhancing the charge transfer rate. Additionally, the high crystallinity of Fe_xO, with its low concentration of defects, preserves the integrity of the crystal structure, thereby effectively improving the material's stability. Additionally, the incorporation of vanadium significantly alters the electronic configuration of the active Fe sites within Fe_xO. This modification enhances the adsorption and desorption processes of oxygen intermediates, ultimately promoting faster reaction kinetics. Consequently, under alkaline conditions, the bifunctional potential gap of V-Fe_xO/NC is only 0.64 V, which outperforms Pt/C+RuO_2 (0.66 V) and surpasses most previously reported bifunctional electrocatalysts. The V-Fe_xO/NC-based ZAB also exhibits excellent performance and durability. This study provides a feasible strategy for tuning catalytic activity by adjusting the crystallinity of metal oxides, which is valuable for the synthesis of highly efficient and stable oxygen electrocatalysts.

Acknowledgements

The authors express their gratitude for the financial support provided by the Natural Science Foundation of Shandong Province of China (ZR2022MB118).

References

1. Z. Wu, Y. Zhang, L. Li, Y. Zhao, Y. Shen, S. Wang, G. Shao, Nitrogen-doped vertical graphene nanosheets by high-flux plasma enhanced chemical vapor deposition as efficient oxygen reduction catalysts for Zn–air batteries. J. Mater. Chem. A. **2020,** 8 (44), 23248-23256.

2. K.-S. Kim, S.-A. Park, H. D. Jung, S.-M. Jung, H. Woo, D. Ahn, S. S. Park, S. Back, Y.-T. Kim, Promoting oxygen evolution reaction induced by synergetic geometric and electronic effects of IrCo thin-film electrocatalysts. ACS Catal. **2022,** 12 (11), 6334-6344.

3. C. Hu, Q. Liang, Y. Yang, Q. Peng, Z. Luo, J. Dong, T. T. Isimjan, X. Yang, Conductivity-enhanced porous N/P co-doped metal-free carbon significantly enhances oxygen reduction kinetics for aqueous/flexible zinc-air batteries. J. Colloid Interface Sci. **2023,** 633, 500-510.

4. X.-L. Chen, J.-W. Huang, Y.-C. Huang, J. Du, Y.-F. Jiang, Y. Zhao, H.-B. Zhu, Efficient Fe-Co-N-C electrocatalyst towards oxygen reductionderived from a cationic coII-based metal–organic framework modified by anion-exchange with potassium ferricyanide. Chemistry – An Asian Journal **2019,** 14 (7), 995-1003.

5. Z. Fan, J. Li, W. Yang, Q. Fu, K. Sun, Y.-C. Song, Z. Wei, Q. Liao, X. Zhu, Green and facile synthesis of iron oxide nanoparticle-embedded N-doped biocarbon as an efficient oxygen reduction electrocatalyst for microbial fuel cells. Chem. Eng. J. **2020,** 385, 123393.

6. T. Zhang, M. Dai, X. Lang, J. Huang, Q. Li, Y. Chen, H. Lin, Self-oxidized amorphous FeO_x@NiO_y electrocatalyst with double-shell hollow nanoarchitecture for boosting oxygen evolution reaction. Ceram. Int. **2024,** 50 (3, Part A), 4415-4422.

7. H. Wu, Y. Li, H. Li, F. Wu, L. Li, X. Xu, Y. Gao, Compressively strained Fe_3O_4 in core—shell oxygen reduction electrocatalyst boosts zinc—air battery performance. Small **2024,** 20 (44), 2404065.

8. S. Qiang, Z. Li, S. He, H. Zhou, Y. Zhang, X. Cao, A. Yuan, J. Zou, J. Wu, Y. Qiao, Modulating electronic structure of CoS_2 nanorods by Fe doping for efficient electrocatalytic overall water splitting. Nano Energy **2025,** 134, 110564.

9. X. Liu, Y. Chen, H. Zhang, L. Zhuo, Q. Huang, W. Zhang, H. Chen, Q. Ling, Synthesis of MXene-based nanocomposite electrode supported by PEDOT:PSS-modified cotton fabric for high-performance wearable supercapacitor. J. Colloid Interface Sci. **2024,** 660, 735-745.

10. B. Zhou, B. Bai, X. Zhu, J. Guo, Y. Wang, J. Chen, Y. Peng, W. Si, S. Ji, J. Li, Insights into effects of grain boundary engineering in composite metal oxide catalysts for improving catalytic performance. J. Colloid Interface Sci. **2024,** 653, 1177-1187.

11. X. Du, J. Huang, J. Zhang, Y. Yan, C. Wu, Y. Hu, C. Yan, T. Lei, W. Chen, C. Fan, J. Xiong, Modulating electronic structures of inorganic nanomaterials for efficient electrocatalytic water splitting. Angew. Chem. Int. Ed. **2019,** 58 (14), 4484-4502.

12. P. Chen, K. Xu, S. Tao, T. Zhou, Y. Tong, H. Ding, L. Zhang, W. Chu, C. Wu, Y. Xie, Phase-transformation engineering in cobalt diselenide realizing enhanced catalytic activity for hydrogen evolution in an alkaline medium. Adv. Mater. **2016,** 28 (34), 7527-7532.

13. W.-J. Jiang, S. Niu, T. Tang, Q.-H. Zhang, X.-Z. Liu, Y. Zhang, Y.-Y. Chen, J.-H. Li, L. Gu, L.-J. Wan, J.-S. Hu, Crystallinity-modulated electrocatalytic activity of a nickel(II) borate thin layer on Ni_3B for efficient water oxidation. Angew. Chem. Int. Ed. **2017,** 56 (23), 6572-6577.

14. J. Zhu, M. Xiao, G. Li, S. Li, J. Zhang, G. Liu, L. Ma, T. Wu, J. Lu, A. Yu, D. Su, H. Jin, S. Wang, Z. Chen, A triphasic bifunctional oxygen electrocatalyst with tunable and synergetic interfacial structure

for rechargeable Zn-air batteries. Adv. Energy Mater. **2020,** 10 (4), 1903003.

15. X. Hu, D. Xia, L. Zhang, J. Zhang, High crystallinity binuclear iron phthalocyanine catalyst with enhanced performance for oxygen reduction reaction. J. Power Sources **2013,** 231, 91-96.

16. T. M. Suzuki, T. Nonaka, A. Suda, N. Suzuki, Y. Matsuoka, T. Arai, S. Sato, T. Morikawa, Highly crystalline β-FeOOH(Cl) nanorod catalysts doped with transition metals for efficient water oxidation. Sustainable Energy & Fuels **2017,** 1 (3), 636-643.

17. Q. Dong, Z. Mo, H. Wang, S. Ji, X. Wang, V. Linkov, R. Wang, N-doped carbon networks containing inserted FeN_x@NC nanospheroids and bridged by carbonnanotubes as enhanced catalysts for the oxygen reductionreaction. ACS Sustainable Chemistry & Engineering **2020,** 8 (18), 6979-6989.

18. F. Huang, X. Chen, H. Sun, Q. Zeng, J. Ma, D. Wei, J. Zhu, Z. Chen, T. Liang, X. Yin, X. Liu, J. Xu, H. He, Atmosphere induces tunable oxygen vacancies to stabilize single-atom copper in ceria for robust electrocatalytic CO_2 reduction to CH_4. Angew. Chem. Int. Ed. **2025,** 64 (3), e202415642.

19. Z. Li, S. Ji, C. Wang, H. Liu, L. Leng, L. Du, J. Gao, M. Qiao, J. H. Horton, Y. Wang, Geometric and electronic engineering of atomically dispersed copper-cobalt diatomic sites for synergistic promotion of bifunctional oxygen electrocatalysis in zinc–air batteries. Adv. Mater. **2023,** 35 (25), 2300905.

20. X. Yang, H. Shen, X. Xiao, Z. Li, Q. Zhou, W. Yang, B. Jiang, Y. Sun, L. Zhang, Z. Yan, Metal nanoparticles decorated CoFe-(oxy)hydroxysulfides nanosheets fabricated by a general strategy for electrocatalytic water splitting. J. Energy Chem. **2025,** 100, 26-38.

21. D. Ye, Y. Shen, H. Mao, Y. Liang, Q. Gao, S. Yang, S. Zhang, X. Cai, Y. Fang, Dual-sources directed construction of N-doped carbon nanotube arrays as superior Self-supported bifunctional air electrodes for Rechargeable/Flexible Zinc-air batteries. Chem. Eng. J. **2023,** 464, 142601.

22. Q. Dong, G. Li, F. Liu, J. Ren, H. Wang, R. Wang, Cu nanoclusters activating ultrafine Fe_3N nanoparticles via the Mott-Schottky effect for rechargeable zinc-air batteries. Appl. Catal. B Environ. Energy **2023,** 326, 122415.

23. M. Kim, H. Nara, Y. Asakura, T. Hamada, P. Yan, J. Earnshaw, M. An, M. Eguchi, Y. Yamauchi, End-to-end pierced carbon nanosheets with meso-holes. Adv. Sci. **2025,** 12 (3), 2409546.

24. A. B. Appiagyei, S. Yang, J. Gu, A. Chaffee, J. Z. Liu, Q. Gu, L. Zhang, Phase segregation-dictated superior Fe-rich ferrite composite for intensified methane dry reforming with CO_2 splitting. Chem. Eng. J. **2025,** 507, 160684.

25. J. Feng, D. Zheng, R. Yin, X. Niu, X. Xu, S. Meng, S. Ma, W. Shi, F. Wu, W. Liu, X. Cao, A wide-temperature adaptive aqueous zinc-air battery-based on Cu–Co dual metal–nitrogen-carbon/nanoparticle electrocatalysts. Small Structures **2023,** 4 (7), 2200340.

26. M. Wang, Q. Dong, S. Ji, H. Wang, J. Peng, X. Wang, V. Linkov, C. Teng, R. Wang, "Coupling-conversion" effect induced by interface-local electric field to improve oxygen reaction kinetics in zinc-air batteries. Chem. Eng. J. **2024,** 481, 148601.

27. Z. Xia, B. Deng, Y. Wang, Z. Jiang, Z.-J. Jiang, Synergistic co-doping induced high catalytic activities of La/Fe doped Co_3O_4 towards oxygen reduction/evolution reactions for Zn–air batteries. J. Mater. Chem. A. **2022,** 10 (44), 23483-23493.

28. J. Chen, Y. Zhuang, Y. Qiao, Y. Zhang, A. Yuan, H. Zhou, Co/Co_7Fe_3 heterostructures with controllable alloying degree on carbon spheres as bifunctional electrocatalyst for rechargeable zinc-air batteries. Int. J. Miner. Metall. Mater. **2025,** 32 (2), 476-487.

29. S. Gopi, A. Panda, A. G. Ramu, J. Theerthagiri, H. Kim, K. Yun, Bifunctional electrocatalysts for water splitting from a bimetallic (V doped-Ni_xFe_y) metal–organic framework MOF@graphene oxide composite. Int. J. Hydrogen Energy **2022,** 47 (100), 42122-42135.

30. Y. Shen, H. Mao, C. Li, K. Li, Y. Liu, J. Liao, S. Zhang, Y. Fang, X. Cai, Unravelling the tip effect of oxygen catalysis in integrated cathode for high-performance flexible/wearable Zn–air batteries. Adv. Fiber Mater. **2024**, 6, 1470-1482.

31. L. Ye, W. Chen, Z.-J. Jiang, Z. Jiang, Co/CoO heterojunction rich in oxygen vacancies introduced by O_2 plasma embedded in mesoporous walls of carbon nanoboxes covered with carbon nanotubes for rechargeable zinc–air battery. Carbon Energy **2024,** 6 (7), e457.

32. Z. Lu, J. Chen, W. Wang, W. Li, M. Sun, Y. Wang, X. Wang, J. Ye, H. Rao, Electrocatalytic, kinetic, and mechanism insights into the oxygen‐reduction catalyzed based on the biomass‐derived FeO_x@N‐doped porous carbon composites. Small **2021,** 17, 2007326.

33. R. Su, X. Tao, K. Zheng, L. Jiao, C. Zhang, R. Yang, H. Xie, X. Meng, C. Xu, Metal-free N, B, F ternary-doped carbon electrocatalyst for boosting the oxygen reduction reaction and high-performance zinc–air battery. Carbon **2024,** 225, 119125.

34. N. He, Y. Sun, X. Chen, J. Wang, G. Liang, F. Mo, Design of S, N-codoped Co–Fe dual-atom sites for efficient alkaline oxygen reduction. J. Mater. Chem. A. **2024,** 12 (17), 10101-10109.

35. Q. Liu, P. Qiao, M. Tong, Y. Xie, X. Zhang, K. Lin, Z. Liang, L. Wang, H. Fu, Enhancing zinc–air battery performance by constructing three-dimensional N-doped carbon coating multiple valence Co and MnO heterostructures. Nano Res. **2024,** 17 (6), 5104-5113.

36. X. Zhang, X. Wen, C. Pan, X. Xiang, C. Hao, Q. Meng, Z. Q. Tian, P. K. Shen, S. P. Jiang, N species tuning strategy in N, S co-doped graphene nanosheets for electrocatalytic activity and selectivity of oxygen redox reactions. Chem. Eng. J. **2022,** 431, 133216.

37. X. Xing, R. Liu, M. Anjass, K. Cao, U. Kaiser, G. Zhang, C. Streb, Bimetallic manganese-vanadium functionalized N,S-doped carbon nanotubes as efficient oxygen evolution and oxygen reduction electrocatalysts. Appl. Catal. B Environ. Energy **2020,** 277, 119195.

38. Y. Wang, J. Wu, S. Tang, J. Yang, C. Ye, J. Chen, Y. Lei, D. Wang, Synergistic Fe−Se atom pairs as bifunctional oxygen electrocatalysts boost low-temperature rechargeable Zn-Air battery. Angew. Chem. Int. Ed. **2023,** 62 (15), e202219191.

39. J. Yang, L. Chang, H. Guo, J. Sun, J. Xu, F. Xiang, Y. Zhang, Z. Wang, L. Wang, F. Hao, X. Niu, Electronic structure modulation of bifunctional oxygen catalysts for rechargeable Zn–air batteries. J. Mater. Chem. A. **2020,** 8 (3), 1229-1237.

40. P. Liu, J. Ran, B. Xia, S. Xi, D. Gao, J. Wang, Bifunctional oxygen electrocatalyst of mesoporous Ni/NiO nanosheets for flexible rechargeable Zn–air batteries. Nano-Micro Letters **2020,** 12 (1), 68.

41. Z. Zhang, Y.-P. Deng, Z. Xing, D. Luo, S. Sy, Z. P. Cano, G. Liu, Y. Jiang, Z. Chen, “Ship in a bottle” design of highly efficient bifunctional electrocatalysts for long-lasting rechargeable Zn–air batteries. ACS Nano **2019,** 13 (6), 7062-7072.

42. B. Ricciardi, W. da Silva Freitas, B. Mecheri, K. U. Nisa, J. Montero, V. C. A. Ficca, E. Placidi, C. Alegre, A. D'Epifanio, Hierarchical porous Fe/Ni-based bifunctional oxygen electrocatalysts for rechargeable zinc-air batteries. Carbon **2024,** 219, 118781.

43. L. Ma, S. Chen, Z. Pei, Y. Huang, G. Liang, F. Mo, Q. Yang, J. Su, Y. Gao, J. A. Zapien, C. Zhi,

Single-site active iron-based bifunctional oxygen catalyst for a compressible and rechargeable zinc–air battery. ACS Nano **2018,** 12 (2), 1949-1958.

44. Z. Cui, G. Fu, Y. Li, J. B. Goodenough, Ni_3FeN-supported Fe_3Pt intermetallic nanoalloy as a high-performance bifunctional catalyst for metal–air batteries. Angew. Chem. Int. Ed. **2017,** 56 (33), 9901-9905.

45. S. Lu, J. Jiang, H. Yang, Y.-J. Zhang, D.-N. Pei, J.-J. Chen, Y. Yu, Phase engineering of iron–cobalt sulfides for Zn–air and Na–ion batteries. ACS Nano **2020,** 14 (8), 10438-10451.

46. W. Cheng, X. Zhao, H. Su, F. Tang, W. Che, H. Zhang, Q. Liu, Lattice-strained metal–organic-framework arrays for bifunctional oxygen electrocatalysis. Nature Energy **2019,** 4 (2), 115-122.

47. T. Tang, W.-J. Jiang, X.-Z. Liu, J. Deng, S. Niu, B. Wang, S.-F. Jin, Q. Zhang, L. Gu, J.-S. Hu, L.-J. Wan, Metastable rock salt oxide-mediated synthesis of high-density dual-protected M@NC for long-life rechargeable zinc–air batteries with record power density. J. Am. Chem. Soc. **2020,** 142 (15), 7116-7127.

48. Y.-S. Wei, M. Zhang, M. Kitta, Z. Liu, S. Horike, Q. Xu, A single-crystal open-capsule metal–organic framework. J. Am. Chem. Soc. **2019,** 141 (19), 7906-7916.

49. X.-T. Wang, T. Ouyang, L. Wang, J.-H. Zhong, T. Ma, Z.-Q. Liu, Redox-inert Fe^{3+} ions in octahedral Sites of Co-Fe spinel oxides with enhanced oxygen catalytic activity for rechargeable zinc–air batteries. Angew. Chem. Int. Ed. **2019,** 58 (38), 13291-13296.

50. H. Liu, P. Li, T. Zhang, Y. Zhu, F. Qiu, Fabrication of recyclable magnetic double-base aerogel with waste bioresource bagasse as the source of fiber for the enhanced removal of chromium ions from aqueous solution. Food Bioprod. Process. **2020,** 119, 257-267.

51. H. Liu, P. Li, F. Qiu, T. Zhang, J. Xu, Controllable preparation of FeOOH/CuO@WBC composite based on water bamboo cellulose applied for enhanced arsenic removal. Food Bioprod. Process. **2020,** 123, 177-187.

52. B. Safdar, Z. Pang, X. Liu, M. A. Jatoi, M. T. Rashid, Optimising deproteinisation methods and effect of deproteinisation on structural and functional characteristics of flaxseed gum. Int. J. Food Sci. Technol. **2020,** 55 (6), 2481-2491.

53. L. Lin, X. Liao, C. Li, M. A. Abdel-Samie, H. Cui, Inhibitory effect of cold nitrogen plasma on Salmonella Typhimurium biofilm and its application on poultry egg preservation. LWT **2020,** 126, 109340.

54. Shazmeen, I. U. Haq, M. S. R. Rajoka, M. Asim Shabbir, M. Umair, I. U. Llah, M. F. Manzoor, A. Nemat, M. Abid, M. R. Khan, R. M. Aadil, Role of stilbenes against insulin resistance: A review. Food Sci Nutr **2021,** 9 (11), 6389-6405.

55. J. Barrio, A. Pedersen, S. C. Sarma, A. Bagger, M. Gong, S. Favero, C.-X. Zhao, R. Garcia-Serres, A. Y. Li, Q. Zhang, F. Jaouen, F. Maillard, A. Kucernak, I. E. L. Stephens, M.-M. Titirici, FeNC oxygen reduction electrocatalyst with high utilization penta-coordinated sites. Advanced Materials **2023,** 35 (14), 2211022.

56. J. Guo, X. Wang, Z. Guo, B. Guo, Z. Wang, Z. Shang, J. Ma, M. Wu, Cu-based active sites supported on nitrogen-rich polymer derived porous carbon fibers as an oxygen reduction electrocatalyst for zinc-air batteries. Carbon **2024,** 228, 119294.

57. H. Lin, L. Zeng, C. Lin, J. Wu, H. He, C. Huang, W. Lai, P. Xiong, F. Xiao, Q. Qian, Q. Chen, J. Lu, Interfacial regulation via configuration screening of a disodium naphthalenedisulfonate additive

enabled high-performance wide-pH Zn-based batteries. Energy Environ. Sci. **2025,** 18 (3), 1282-1293.

58. M. Kim, R. Xin, J. Earnshaw, J. Tang, J. P. Hill, A. Ashok, A. K. Nanjundan, J. Kim, C. Young, Y. Sugahara, J. Na, Y. Yamauchi, MOF-derived nanoporous carbons with diverse tunable nanoarchitectures. Nat. Protoc. **2022,** 17 (12), 2990-3027.

59. M. Kim, K. L. Firestein, J. F. S. Fernando, X. Xu, H. Lim, D. V. Golberg, J. Na, J. Kim, H. Nara, J. Tang, Y. Yamauchi, Strategic design of Fe and N co-doped hierarchically porous carbon as superior ORR catalyst: from the perspective of nanoarchitectonics. Chem. Sci. **2022,** 13 (36), 10836-10845.